

## Influence of heat treatment on the microstructure of a sintered bronze-aluminum alloy

<http://dx.doi.org/10.1590/0370-44672023770004>

**Eduardo Serafim Silva**<sup>1,4</sup>

<https://orcid.org/0000-0001-5628-045X>

**Elioenai Levi Barbedo**<sup>2,5</sup>

<https://orcid.org/0000-0001-9342-0589>

**Alexandre Nogueira Ottoboni Dias**<sup>2,6</sup>

<https://orcid.org/0000-0003-0989-9350>

**Daniela Sachs**<sup>1,7</sup>

<https://orcid.org/0000-0002-3767-2455>

**Gilbert Silva**<sup>2,8</sup>

<https://orcid.org/0000-0002-3923-3982>

**Alfeu Saraiva Ramos**<sup>3,9</sup>

<https://orcid.org/0000-0002-4520-3114>

<sup>1</sup>Universidade Federal de Itajubá – UNIFEI, Instituto de Física e Química– IFQ, Itajubá – Minas Gerais –Brasil.

<sup>2</sup>Universidade Federal de Itajubá – UNIFEI, Instituto de Engenharia Mecânica– IEM, Itajubá –Minas Gerais –Brasil.

<sup>3</sup>Universidade Federal de Alfenas - UNIFAL-MG, Programa de Pós-Graduação em Ciência e Engenharia de Materiais – PPGCEM, Alfenas – Minas Gerais - Brasil.

E-mails: <sup>4</sup>[eduardoserafim18@unifei.edu.br](mailto:eduardoserafim18@unifei.edu.br),

<sup>5</sup>[levibarbedo@unifei.edu.br](mailto:levibarbedo@unifei.edu.br), <sup>6</sup>[aottoboni@unifei.edu.br](mailto:aottoboni@unifei.edu.br),

<sup>7</sup>[danisachs@unifei.edu.br](mailto:danisachs@unifei.edu.br), <sup>8</sup>[gilbert@unifei.edu.br](mailto:gilbert@unifei.edu.br),

<sup>9</sup>[alfeu.ramos@unifal-mg.edu.br](mailto:alfeu.ramos@unifal-mg.edu.br)

### Abstract

When processed conventionally, aluminum-bronze alloys with high mechanical strength require machining after the raw state of fusion, and the waste (chips), if not reused, can cause problems for the environment and costs for the company. Therefore, this article proposes an alternative for recycling aluminum bronze through the new route via Powder Metallurgy (PM), analyzing the resulting microstructure. This study compares the microstructures of the aluminum bronze derived from extraction (the samples received - SR) and the state after the powder metallurgy (PM) process with the addition of vanadium carbides (VC). The study also analyzes the distribution of VC in the microstructure of the PM composite as well as the influence of the TQ30 heat treatment on this composite. For the PM process, aluminum alloy and bronze chips were ground together with vanadium carbide (VC) in a high-energy mill for 50 hours. The powders obtained were pressed uniaxially (400 MPa) to achieve good compaction. The samples were then sintered (900°C/1h), water quenched (900°C/2h), and subjected to treatment according to the TQ30 standard, which, in addition to the previous treatments, also includes tempering at 500°C for 2 hours (ASTM B150/B150M-12 standard). The microstructure observed in the SR samples was martensitic (in needles), with secondary phases dispersed in the matrix. On the other hand, the microstructure of the PM samples showed equiaxed grains of the alpha phase ( $\alpha$ ), as well as the secondary phases kapa ( $\kappa$ ) and beta line ( $\beta'$ ), in contrast to the needle-shaped microstructure of the conventional melting process.

**Keywords:** Aluminum bronze; sintering process; powder metallurgy; microstructure; composite.

## 1. Introduction

Rapid development and the search for high-yield results at minimum cost have always required the industrial sector to search for increasingly resistant, lighter-weight and better cost-effective materials. With this competitiveness, a significant evolution of materials and manufacturing processes used in the industry has been observed over time. These evolutions are often based on the microstructure of materials (Dias *et al.*, 2018; Xu, X.; Zhao, H., *et al.*, 2022).

High productivity in the manufacture of large quantities of identical parts, energy savings, the simplification or elimination of finishing operations, the fact that only 3% of the initial raw material is commonly wasted with the finished part, not generating scrap, and the high wear resistance all provide a relative PM advantage compared to conventional processes, such as casting. Such benefits of this process translate into high energy savings, quality, and added value of the final products (Dias *et al.*, 2018; Wang *et al.*, 2018).

The high-energy milling and sintering processes can generate energy savings in the production of parts and components, in

addition to offering environmental benefits, since they use metal chips processed in conventional machining in order to present final products with excellent physical and mechanical properties (high mechanical resistance) in a sustainable way when compared to cast materials (Hai-Dong, Hao-Wei, Liang, 2013; Jabur, 2013).

Therefore, the aluminum bronze alloy, used in several applications at a high cost, is an excellent choice to explore alternative routes that may bring benefits not yet seen. Its choice in noble engineering projects is precisely because its mechanical resistance is equivalent to that of many high-strength steels and its corrosion resistance is compatible with that of stainless steels (ASM Handbook, 1993; Xu, X.; Zhao, H., *et al.*, 2022).

With regard to heat treatments of aluminum bronze, it can be said that, in addition to stress relief and annealing treatments, others that stand out are solubilization and precipitation hardening (Freitas, 2014).

As reported in numerous previous works, the characteristic microstructure of aluminum bronze is constituted by the phases alpha ( $\alpha$ ), and beta ( $\beta$ ), in

addition to the secondary phases kappa ( $\kappa$ ) according to the heat treatment submitted (Tavares, S. S. M., *et al.*, 2021; Xu, X.; Zhao, H., *et al.*, 2022).

After casting, tempering provides greater resistance to the cast material. The tempered material, on the other hand, generates precipitates that further increase the magnitude of its hardness. In casting, due to the high aluminum content of these alloys, it is necessary to use adequate heat treatment to obtain good mechanical properties (Phillips, 1945; Tavares, S. S. M., *et al.*, 2021).

The range of the Cu-Al diagram that has approximately 12% aluminum is extensively explored (Fig. 1a). Because in this range there is a eutectoid point "R" where the transition from the  $\beta$  phase to the  $\alpha+\gamma_2$  phases occurs at temperatures close to 565°C. But, during heating up to 900°C and rapid cooling, the  $\beta$  phase transforms into the metastable martensitic phase  $\beta'$ , due to its acicular or needle shape. This phase also increases the mechanical properties of the alloy. However, further treatment is required to decrease its brittleness. (Coutinho, 1980; Barr, C.; Andrey, P., *et al.*, 2022).

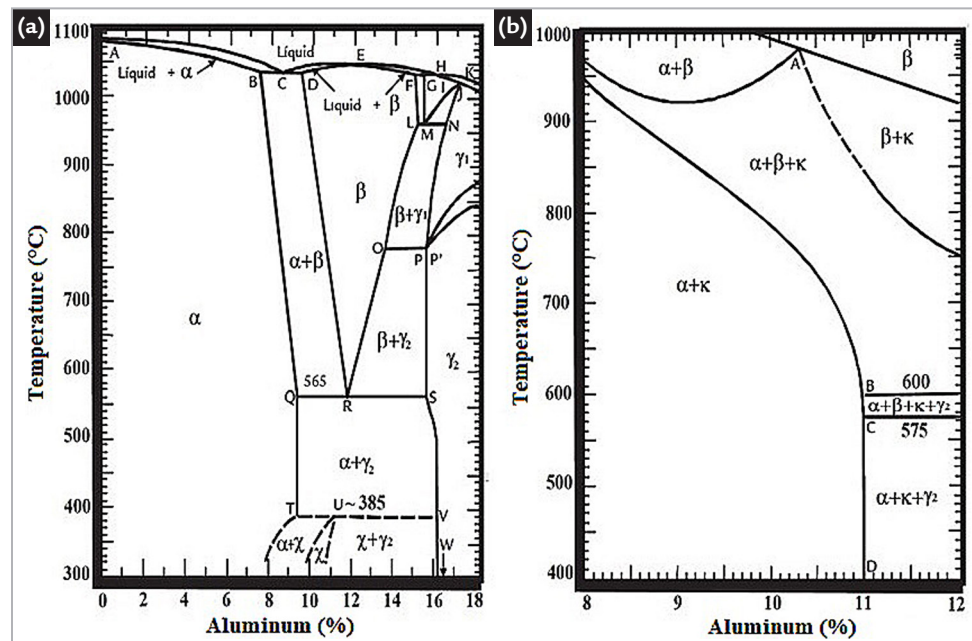


Figure 1 - a) Binary aluminum-bronze balance diagram; b) Equilibrium diagram of aluminum bronze with the addition of Fe and Ni. (adapted from Rodrigues *et al.*, 2012).

The aluminum content is mainly responsible for the different transformations that occur in this type of material. However, the addition of nickel and iron to the Cu-Al alloy increases the stability of the  $\alpha$  phase and decreases the formation of the  $\beta$  phase (Fig. 1b). These two elements significantly increase the mechanical prop-

erties of the Cu-Al-Fe-Ni alloy due to the formation of  $\alpha$ ,  $\beta$  phases and intermetallic precipitates called "k phases". (kI, kII, kIII e kIV), which, depending on chemical composition and heat treatment, can be  $\text{Fe}_3\text{Al}$ ,  $\text{FeNi}$ ,  $\text{FeAl}$ , or  $\text{NiAl}$  (Wharton, 2008; Rodrigues *et al.*, 2012; Barr, C.; Andrey, P., *et al.*, 2022).

The main objective of this study is to carry out the microstructural characterization of a composite produced by the PM route (using high-energy milling with the addition of VC, from bronze-aluminum alloy chips) for comparison purposes with the material used in the industry, obtained via conventional melting processes.

## 2. Materials and methods

### 2.1 Powder Preparation

The aluminum-bronze alloy powders were obtained from the high-energy milling of chips (residues or scraps) from the machining process of aluminum-bronze bars obtained by conventional casting. The nominal composition of this alloy is: 73.60% Cu, 12.69% Al, 7.20% Fe, 4.87% Ni, and 0.94% Mn (% in weight), similar to the ASTM C63020 grade.

### 2.2 Compacting/Sintering/TQ30

For each sample, 1g of ground material was compacted in a cylindrical matrix with an opening of 8 mm (VC131), adding 1% zinc stearate (binder). A load of 400 MPa (2t) was used for 30 seconds, three consecutive times. Compaction took place in a uniaxial hydraulic press (SCHULZ; capacity: 15t).

### 2.3 Microstructural analyzes

The microstructures of the samples were characterized by an MO (Optical Microscope) "Carl Zeiss Jenavert<sup>®</sup>", with a digital camera, and an image analyzer ("Image Pro-Plus<sup>®</sup>").

Sanding was done with SiC-based sandpaper in the sequences of 600, 800,

Milled were 30g of aluminum bronze chips in a ball-to-weight ratio of 1:20, with the addition of 3% (by weight) of VC and 1% (by weight) of Stearic Acid (ACP). The process took place for 50 hours, with a stop at 15-minute intervals for each hour of work, with unidirectional rotations of 350 rpm through the planetary ball mill NQM 0.3L/Noah-Nuoya Corp, in an

The green samples were sintered in a 3000/3P-S furnace with a controlled atmosphere (vacuum, 10-2 mbar). The set was heated at a rate of 10°C/min to a temperature of 400°C, remaining at this temperature for 15 minutes, for the evaporation of organic products (binders). Then (at the same rate), it was heated to a sintering temperature of

and 1200 mesh. The polishing took place with the use of alumina (1µm).

For the chemical attack, a solution of ferric chloride (5%) and hydrochloric acid (5%) was used between 2 and 5 seconds.

The morphology of the aluminum bronze powders and the distribu-

tion of carbides were analyzed by a SEM (Scanning Electron Microscope), "Carl Zeiss EVO<sup>®</sup> MA15 SEM," using secondary electron (SE) detectors, as well as backscattered electrons (BSD). In addition, an energy dispersive x-ray analysis (EDS) was performed.

These parameters were chosen through DoE (Design of Experiments), published by DIAS, A. N. O. *et al.*, 2019.

The aluminum bronze bar samples were kindly provided by the company ELEB Equipamentos LTDA. Vanadium carbide, whose granulometry varies from 3 to 4 µm, was produced by Hermann C. Starck.

900°C, remaining for another 1 hour. Finally, the samples were cooled inside the oven.

After that, quenching (900°C for 2 hours and cooling in water) and quenching-tempering (TQ30), treatments were carried out on the sintered samples, with tempering at 500°C for 2 (ASTM B150/B150M-12 standard).

## 3. Results and discussion

In Fig. 2, the microstructure of foundry-derived aluminum bronze (SR) is shown. It was necessary to know this micrograph before the chemical attack so that the presence of precipitates can be more easily identified. This is because, for some special alloys, the chemical attack itself

removes many of these precipitates, making their perfect identification impossible.

Still in Fig. 2, it is observed that the k-type precipitates (Fe<sub>3</sub>Al, FeNi, FeAl, or NiAl) are organized in a well-distributed manner in the aluminum-bronze matrix in the SR state.

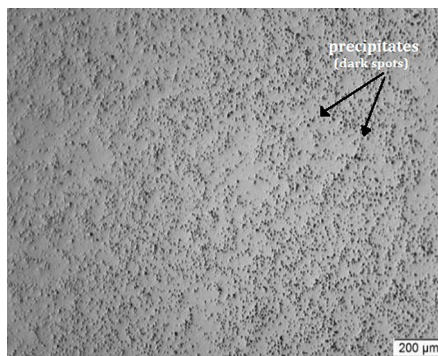


Figure 2 - Micrograph of aluminum bronze in the SR state obtained via MO of precipitates, before chemical attack with ferric chloride. 50x magnification.

It can be seen that by heating the aluminum-bronze alloy to the temperature of the beta phase (β) and submitting it to

subsequent cooling in water, there is an impediment to the complete transformation of this phase. The result is just a deforma-

This is due to the quenching and tempering heat treatments (TQ30) to which this material is subjected after melting. It should be noted that the SR material does not have pores, and even if there were, these would be blurred spots of grayish coloration.

mation on the crystalline layer caused by sliding of adjacent crystallographic planes, giving rise to a new constituent called β'

and precipitation in the form of alpha solid solution needles (apro-proeutectoid)

seen in Fig. 3. Subsequently, there is the transformation of  $\beta' \rightarrow \alpha'1$  ("pure" mar-

tensite). This behavior can be improved by martensitic treatment.

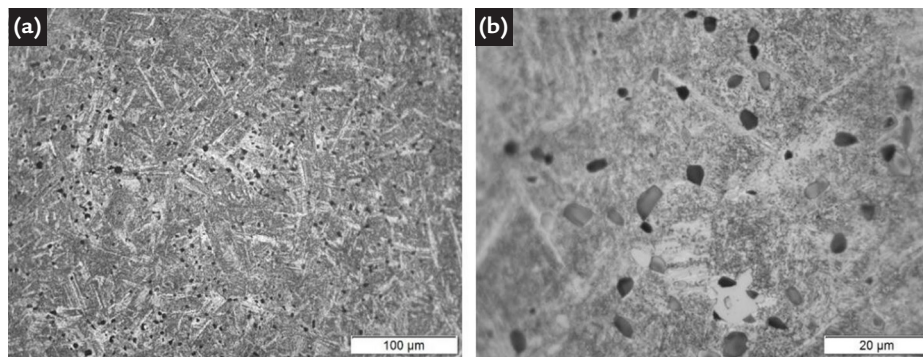


Figure 3 - Micrograph of the aluminum bronze alloy in the SR state obtained by MO. Chemical attack with ferric chloride for 5s. Increases: a) 200x; b) 1,000x.

In Fig. 4, Paul R. Howell can be seen more clearly when the material in the SR state is subjected to the tempering heat treatment after quenching during its manufacturing process.

However, due to the high aluminum

content (> 12% Al) detected in the SR material, the phases involved cannot be accurately stated. But, according to Paul R. Howell (2000), the presence of bainite ( $\alpha B$ ), commonly seen in these complex alloys with high aluminum content after temper-

ing at 500°C and cooling in air, suggests that there is a possible additional eutectoid phase ( $\alpha + \gamma_2$ ). In general, the structure is predominantly acicular dendritic, typical of aluminum bronze after tempering, and the nomenclature varies from author to author.

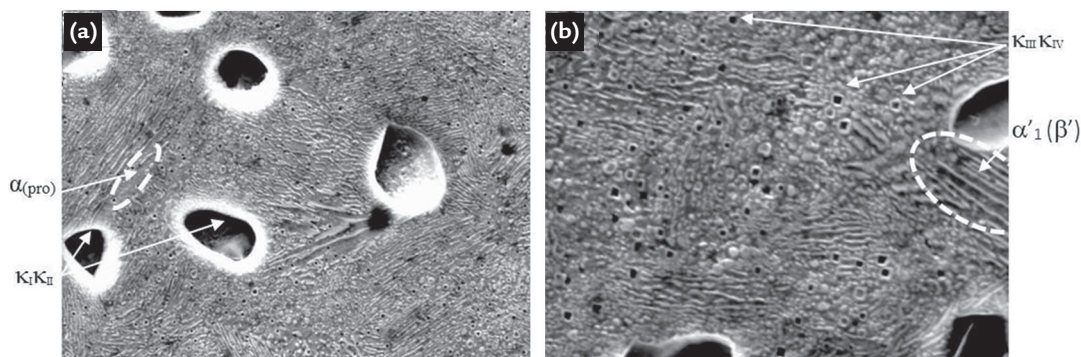


Figure 4 - Micrograph of the aluminum-bronze alloy in the SR state, obtained via SEM-SE, with ferric chloride attack for 5 seconds. Increases: a)10,000x; b)20,000x.

The  $\alpha$  phase is richer in copper and more ductile than the  $\beta'$  (martensitic) phase. The  $\kappa$  phase varies according to the amounts of iron and nickel. The constituent precipitates of  $\kappa$  phase (lighter) are rich in

nickel (Ni), whereas the darker constituents are rich in iron (Fe). In summary,  $Fe_3Al$  ( $\kappa I$ ) are larger nodules, rich in Fe, which have  $FeNi$  ( $\kappa II$ ) rich in nickel. The smaller particles are probably based on  $FeAl$ ,  $NiAl$ ,

or combinations of these. These details are seen in Fig. 5, through SEM-EDS analysis of the material in the SR state, checking the amount of elements present, eliminating the possibility that they are just pores.

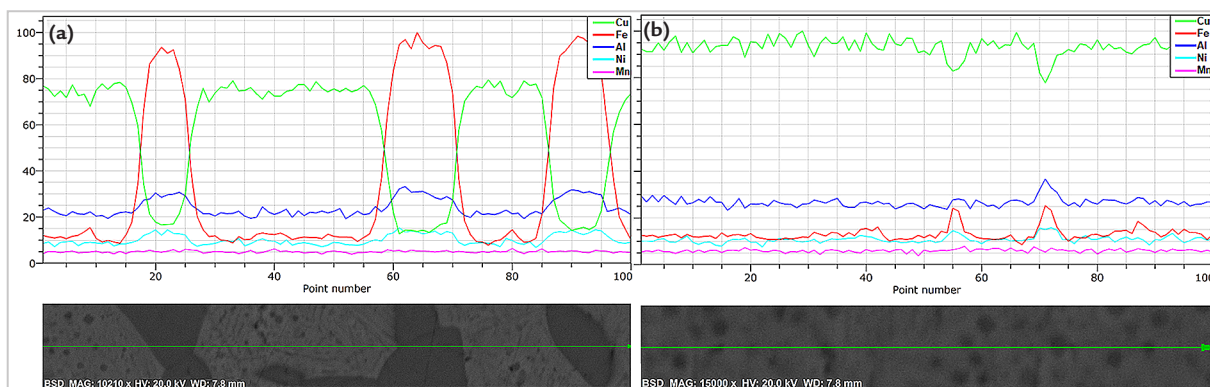


Figure 5 - a) Analysis of SEM-EDS (Line Scan) in the SR state - precipitates  
b) Analysis of SEM-EDS (Line Scan) in the SR state - minor precipitates.

Figs. 6 and 7 show SEM-EDS (line scan) analyses of the material processed

through PM. The matrices are basically com-

posed of copper and aluminum (as expected). However, the concentration

of aluminum and other elements in the particle boundaries was noted. The lighter phases are rich in copper and

have less iron and aluminum. On the other hand, the darker phases are made up of kappa phases (fine precipitates)

and other secondary phases due to variations in the peaks identifying the elements Fe, Al, Ni, C, and V.

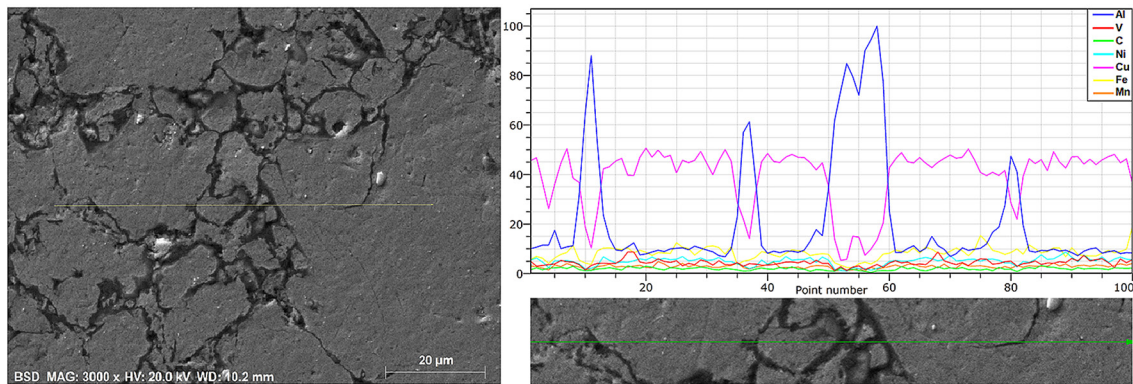


Figure 6 - SEM- (BSD and EDS) Analysis (Line Scan) in aluminum bronze only tempered.

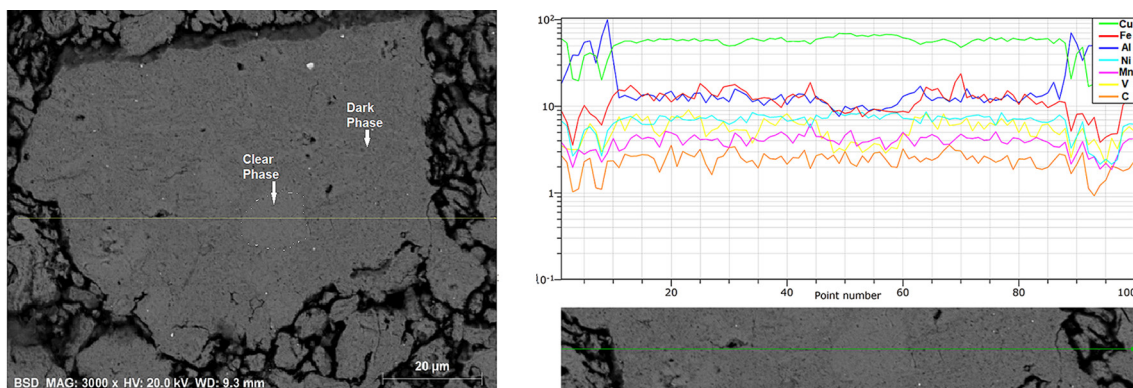


Figure 7 - SEM-(BSD and EDS) analysis (Line Scan) on aluminum bronze TQ30.

Figs. 8, 9, and 10 present the micrographs (MO), through a broader view of the aluminum bronze processed via PM. They consist of the micrographs of the three conditions (sintered, sintered-hardened, and sintered-hardened-tempered / TQ30), all pressed in a uniaxial press.

It can be noticed that the samples are only sintered (Fig. 8), and the matrices are basically constituted of  $\alpha$  phase (more ductile) with large par-

ticles. Darker regions close to particle boundaries are secondary/intermetallic phases, poorly distinguished by MO. It is also observed that a large number of pores (out of focus regions) are larger and more evenly distributed in this matrix, which is typical of a post-sintering material via PM.

Figs. 9 and 10 are LM micrographs of the sintered-tempered samples and TQ30-treated samples, respectively. These samples became thicker, indicat-

ing a preference for sheltering secondary phases, such as the kappa phase, for example, more refined by the PM process.

In relation to the TQ30 material (which, in addition to being sintered and quenched, was also tempered at 500°C with air cooling), the difference is in the precipitation of the secondary phases over the entire matrix. This confirms the aging process and can cause a significant increase in the hardness value.

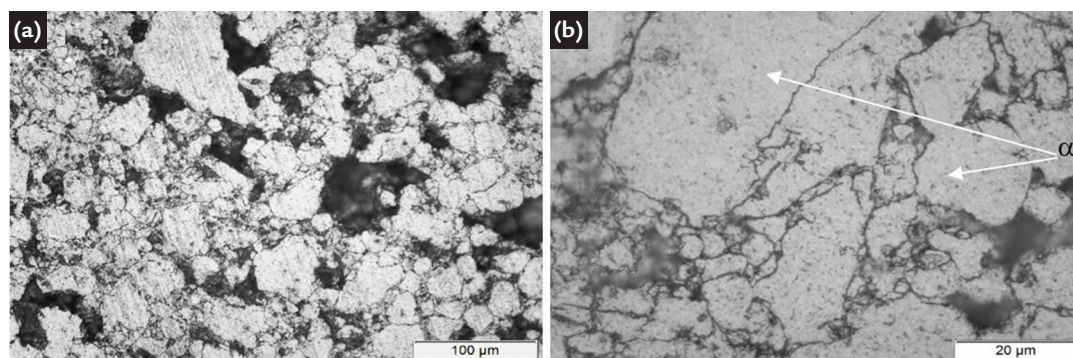


Figure 8 - MO micrograph of bronze-sintered aluminum. Chemical attack with ferric chloride for 1 s. Magnifications: (a) 200x; (b) 1,000x.

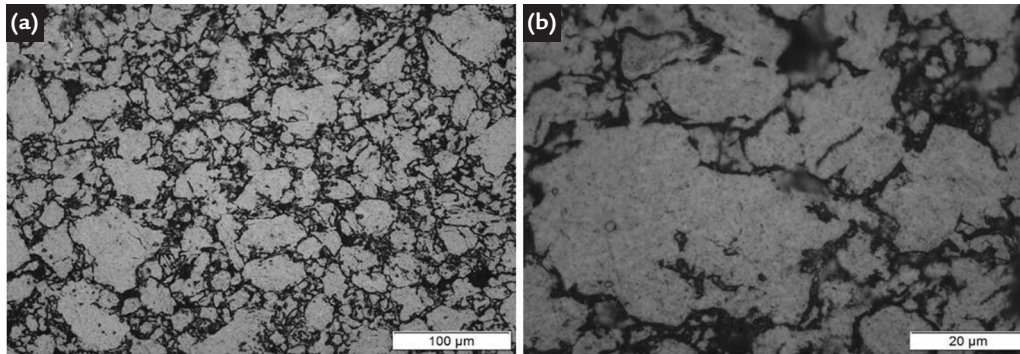


Figure 9 - MO micrograph of bronze-sintered-hardened aluminum. Chemical attack with ferric chloride for 1s. Magnifications: a) 200x; b) 1,000x.

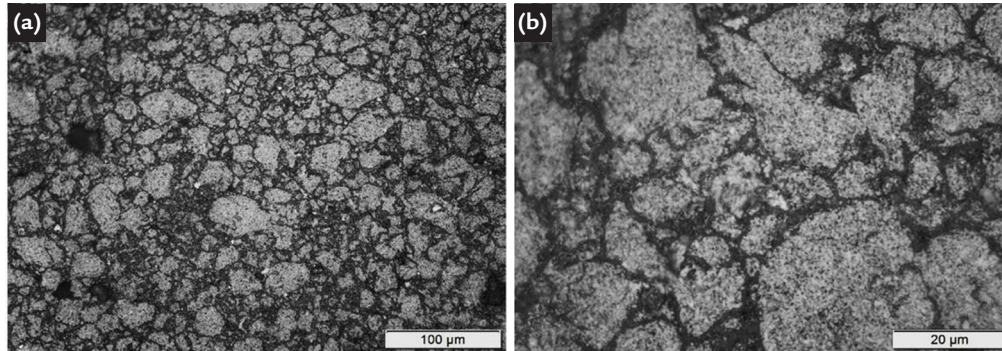


Figure 10 - MO micrograph of aluminum bronze TQ30. Chemical attack with ferric chloride for 1s. Magnifications: a) 200x; b) 1,000x.

The SEM-SE analysis of Fig. 11 for the three cases studied expanded the details already seen in MO. The contour regions, shown to prevent the excessive growth of particles and the evolution of these particles, start during

sintering (Fig. 11a), increase in size after quenching (Fig. 11b), and stabilize with smaller and more defined sizes after TQ30 (Fig. 11c). It should be mentioned that the lighter spots, identified in Fig. 11c, were contaminated by silica,

due to the sand that is used to completely clean the jars. It should be mentioned that the lighter spots, identified in Fig. 11c, were contaminated by silica, due to the sand that is used to completely clean the jars.

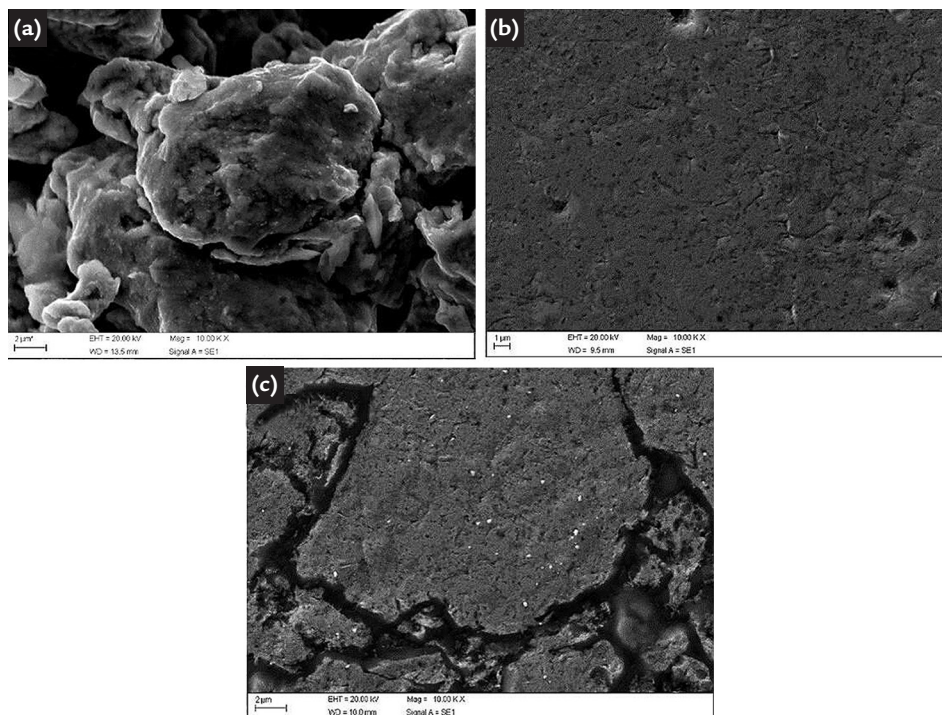


Figure 11 - SEM-SE analysis. Tempered aluminum bronze, etched (ferric chloride) for 1s. 10,000x magnification. a) interior morphology of the sinter; b) Temperate morphology; c) TQ30 morphology.

Fig. 12 shows the distribution of VC over the sintered matrix. Note that, after milling and sintering (with the established parameters), these carbides

are evenly distributed and can be seen as tiny particles aggregated on the surface.

The well-distributed presence of these carbides also helps in the magni-

tude of the final hardness of aluminum bronze processed through PM.

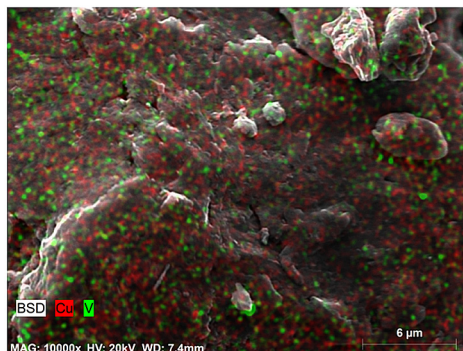


Figure 12 - Distribution of VC on the sintered aluminum bronze matrix. 10,000x magnification BSD (EDS).

#### 4. Conclusion

The microstructure derived from the conventional melting process (material as received - SR) was shown to be martensitic (needle-shaped) with secondary phases dispersed in the matrix.

On the other hand, the microstructure obtained through the PM process, demonstrated to have equiaxed grain shapes of  $\alpha$  phases, in addition to the kappa and  $\beta'$  secondary phases, different from those needle shapes of the conventional melting process.

Coarse kappa precipitates are shown to be more common in foundry processes. On the other hand, what is perceived in

relation to the MP process is a finer precipitation of kappa phases after the TQ30 heat treatment and this can greatly influence the mechanical strength of this material.

SEM/EDS analysis showed that  $\text{Fe}_3\text{Al}$  ( $\kappa\text{I}$ ) are larger nodules, rich in Fe, which have  $\text{FeNi}$  ( $\kappa\text{II}$ ) rich in nickel inside. Smaller particles are based on  $\text{FeAl}$ ,  $\text{NiAl}$  or their combinations for SR materials.

The material via PM, on the other hand, consists of well-refined and well-distributed precipitates in the matrix, like the VC. However, it is noticed that mainly aluminum is present, preferen-

tially in the grain boundaries (places of high energy).

This is due to the fact that only this element experiences the liquid phase (due to its low melting point) in the sintering process. A better distribution of these aluminum particles can be seen in the matrix after the TQ30 heat treatment, when more time is allowed for their diffusion inside the matrix.

Finally, VC, used in the high-energy milling of aluminum bronze, proved to be an excellent option to help with comminution/milling, in addition to being very well distributed over the matrix.

#### Acknowledgements

The authors acknowledge the Brazilian agencies CAPES and FAPEMIG by the financial support and also UNIFEL.

#### References

- ASTM. *B962-17. Standard test methods for density of compacted or sintered powder metallurgy (PM) products using archimedes' principle*. ASTM International, West Conshohocken, PA, USA, 2017. Disponível em: [www.astm.org](http://www.astm.org).
- BARR, C.; ANDREY, P.; DAVID, M.; MILAN, C.; BRANDT, M. *et al.* Effect of composition on the tensile and corrosion performance of nickel aluminium bronze produced via laser powder bed fusion. *Additive Manufacturing*, v. 54, 2022.
- COUTINHO, T. de A. Cobre e Suas Ligas: análise e prática. *In: Metalografia de não-ferrosos*. São Paulo: Edgard Blucher, cap. 3, p. 46-47, 1980.
- DIAS, A. N. O. *et al.* Comparative analysis of niobium and vanadium carbide efficiency in the high energy mechanical milling of aluminum bronze alloy. *REM - Int. Eng. Journal*, v. 71, p. 59-65, 2018.
- DIAS, A. N. O.; RODRIGUES, G.; MENDONÇA, C. S. P.; SILVA, G. Analysis of the densification of a composite obtained by sintering process of aluminum bronze powders with different carbides. *REM - Int. Eng. Journal*, v. 72, n. 3, jul./set., 2019.
- DIAS, A. N. O. *et al.* Effect of high energy milling time of the aluminum bronze alloy obtained by powder metallurgy with niobium carbide addition. *Materials Research*, v. 20, p. 747-754, 2017.
- DOTTER, R. T. Blending and premixing of metal powders. *ASM Handbook - Powder Metallurgy*, v. 7, 1993.
- FREITAS, P. S. *Tratamento térmico dos metais: da teoria à prática*. São Paulo: Editora SENAI, 2014. cap 9, p. 119-126.
- GERMAN, R. M. *Powder metallurgy and particulate materials processing: the processes, materials, products, properties and applications*. Princeton, USA: Metal Powder Industries Federation, p. 522, 2005.

- HAI-DONG, X., HAO-WEI, Y., LIANG, Z. Research on powder metallurgy gear lifting fire tanker performance. *Procedia Engineering*, v. 52, p. 453- 457, 2013.
- HOSSEIN-ZADEH, M. *et al.* Synthesis and structural evolution of vanadium carbide in nanoscale during mechanical alloying. *Journal of King Saud University - Engineering Sciences*, v. 28, p. 207-212, 2016.
- HOWELL, P. R. *On the phases microconstituents in nickel-aluminum bronzes*. Copper Development Association Inc., 2000.
- JABUR, A. S. Effect of powder metallurgy conditions on the properties of porous bronze. *Powder Technology*, v. 237, p. 477-483, 2013.
- KLAR, E.; SAMAL, P. *Powder metallurgy stainless steels: processing, microstructures, and properties*. Materials Park, Ohio, USA: ASM International, p. 243, 2007.
- LV, Y. *et al.* Effect of post heat treatment on the microstructure and microhardness of friction stir processed NiAl bronze alloy. *Metals*, v. 5, p. 1695-1703, 2015.
- PHILLIPS, A. *Metais e ligas não ferrosos: propriedades e empregos*. São Paulo: Escola Politécnica da USP, 1945.
- RODRIGUES, *et al.* Caracterização de uma liga de bronze de alumínio submetida a diferentes tratamentos térmicos. *Rem: Rev. Esc. Minas*, v. 65, n. 3, p. 343-348, 2012. ISSN 0370-4467.
- ROSARIO FRANCIA, S. R.; VILLACORTA ARÉVOLO, L.; FALCONI ROSÁDIO, V.; RENGIFO SING, W. Tratamiento térmico de los bronzes aluminio complejos, transformación martensítica y la fase kappa – templabilidad. *Revista del Instituto de Investigación de la Facultad de Minas, Metalurgia y Ciencias Geográficas*, v. 14, n. 27, 2011.
- SURYANARAYANA, C. Mechanical alloying and milling. *Progress in Materials Science*, V. 46, n. 1-2, p. 1-184, 2001.
- TAVARES, S. S. M.; MOTA, N. M.; DA IGREJA, H. R.; BARBOSA, C.; PARDAL, J. M. Microstructure, mechanical properties, and brittle fracture of a cast nickel- aluminum-bronze (NAB) UNS C95800. *Engineering Failure Analysis*, v. 128, 2021.
- WANG, W. *et al.* Numerical simulation of densification of Cu–Al mixed metal powder during axial compaction. *Metals*, v. 8, p. 537, 2018.
- WHARTON, J. A.; STOKES, K. R. The influence of nickel-aluminum bronze microstructure and crevice solution on the initiation of crevice corrosion. *Electrochimica Acta*, v. 53, p. 2463-2473, 2008.
- XU, X.; ZHAO, H.; HU, Y.; ZONG, L.; QIN, J.; ZHANG, J. *et al.* Effect of hot compression on the microstructure evolution of aluminium bronze alloy. *Journal of Materials Research and Technology*, v. 19, p. 3760-3776, 2022.

---

Received: 25 January 2023 - Accepted: 15 November 2023.

